

Measurement of Neutrino Flux from Neutrino-Electron Elastic Scattering

J. Park,¹ L. Aliaga,² O. Altinok,³ L. Bellantoni,⁴ A. Bercellie,¹ A. Bodek,¹ A. Bravar,⁵ H. Budd,¹ M.F. Carneiro,⁶ J. Chvojka,¹ S.A. Dytman,⁷ B. Eberly,^{7,*} J. Felix,⁸ L. Fields,^{4,9} A.M. Gago,¹⁰ R.Galindo,¹¹ A. Ghosh,^{6,1} T. Golan,^{1,4} R. Gran,¹² D.A. Harris,⁴ T. Le,^{3,13} J. Kleykamp,¹ E. Maher,¹⁴ S. Manly,¹ Nuruzzaman,¹¹ W.A. Mann,³ C.M. Marshall,¹ D.A. Martinez Caicedo,^{4,†} K.S. McFarland,^{1,4} C.L. McGivern,⁷ J. Miller,¹¹ A. Mislivec,¹ J.G. Morfín,⁴ J. Mousseau,^{15,‡} D. Naples,⁷ J.K. Nelson,² A. Norrick,² J. Osta,⁴ V. Paolone,⁷ C.E. Patrick,⁹ G.N. Perdue,^{4,1} L. Rakotondravohitra,^{4,§} H. Ray,¹⁵ L. Ren,⁷ D. Rimal,¹⁵ P.A. Rodrigues,¹ D. Ruterbories,¹ H. Schellman,^{16,9} C.J. Solano Salinas,¹⁷ N. Tagg,¹⁸ B.G. Tice,¹³ E. Valencia,⁸ T. Walton,^{19,¶} J. Wolcott,^{1,**} M.Wospakrik,¹⁵ G. Zavala,⁸ and D. Zhang²

(The MINERvA Collaboration)

¹University of Rochester, Rochester, New York 14610 USA

²Department of Physics, College of William & Mary, Williamsburg, Virginia 23187, USA

³Physics Department, Tufts University, Medford, Massachusetts 02155, USA

⁴Fermi National Accelerator Laboratory, Batavia, Illinois 60510, USA

⁵University of Geneva, Geneva, Switzerland

⁶Centro Brasileiro de Pesquisas Físicas, Rua Dr. Xavier Sigaud 150, Urca, Rio de Janeiro, RJ, 22290-180, Brazil

⁷Department of Physics and Astronomy, University of Pittsburgh, Pittsburgh, Pennsylvania 15260, USA

⁸Campus León y Campus Guanajuato, Universidad de Guanajuato, Lascruain de Retana No. 5, Col. Centro. Guanajuato 36000, Guanajuato México.

⁹Northwestern University, Evanston, Illinois 60208

¹⁰Sección Física, Departamento de Ciencias, Pontificia Universidad Católica del Perú, Apartado 1761, Lima, Perú

¹¹Departamento de Física, Universidad Técnica Federico Santa María, Avda. España 1680 Casilla 110-V, Valparaíso, Chile

¹²Department of Physics, University of Minnesota – Duluth, Duluth, Minnesota 55812, USA

¹³Rutgers, The State University of New Jersey, Piscataway, New Jersey 08854, USA

¹⁴Massachusetts College of Liberal Arts, 375 Church Street, North Adams, MA 01247

¹⁵University of Florida, Department of Physics, Gainesville, FL 32611

¹⁶Department of Physics, Oregon State University, Corvallis, Oregon 97331, USA

¹⁷Universidad Nacional de Ingeniería, Apartado 31139, Lima, Perú

¹⁸Department of Physics, Otterbein University, 1 South Grove Street, Westerville, OH, 43081 USA

¹⁹Hampton University, Dept. of Physics, Hampton, VA 23668, USA

(Dated: August 20, 2022)

Muon-neutrino elastic scattering on electrons is an observable neutrino process whose cross section is precisely known. Consequently a measurement of this process in an accelerator-based ν_μ beam can improve the knowledge of the absolute neutrino flux impinging upon the detector; typically this knowledge is limited to $\sim 10\%$ due to uncertainties in hadron production and focusing. We have isolated a sample of 135 ± 17 neutrino-electron elastic scattering candidates in the segmented scintillator detector of MINERvA, after subtracting backgrounds and correcting for efficiency. We show how this sample can be used to reduce the total uncertainty on the NuMI ν_μ flux from 9% to 6%. Our measurement provides a flux constraint that is useful to other experiments using the NuMI beam, and this technique is applicable to future neutrino beams operating at multi-GeV energies.

PACS numbers: 13.15.+g,13.66-a

Neutrino-electron elastic scattering is precisely predicted in the electroweak Standard Model because it involves only the scattering of fundamental leptons. At tree level and in the limit that the neutrino energy E_ν is much greater than the electron mass m_e , the $\nu e \rightarrow \nu e$ cross section for all active neutrinos and antineutrinos is given generically by

$$\frac{d\sigma(\nu e^- \rightarrow \nu e^-)}{dy} = \frac{G_F^2 s}{\pi} [C_{LL}^2 + C_{LR}^2(1-y)^2], \quad (1)$$

where G_F is the Fermi weak coupling constant, s is the Mandelstam invariant representing the square of the total

energy in the center-of-mass frame, and $y \equiv T_e/E_\nu$ where T_e is the electron kinetic energy. The couplings C_{LL} and C_{LR} depend on the neutrino flavor and whether the incident particle is a neutrino or anti-neutrino. For ν_μ and ν_τ , $C_{LL} = \frac{1}{2} - \sin^2 \theta_W$ and $C_{LR} = \sin^2 \theta_W$, where θ_W is the Weinberg angle, and for the corresponding anti-neutrinos the values for C_{LL} and C_{LR} are interchanged. For ν_e ($\bar{\nu}_e$), the value of C_{LL} (C_{LR}) is $\frac{1}{2} + \sin^2 \theta_W$ because the interaction contains interfering contributions from the neutral current interaction that is present for all flavors and from a charged-current interaction that is present only for electron neutrinos. The kinematics of

the reaction limit the magnitude of the four-momentum transferred from the neutrino, q , to be less than \sqrt{s} . The angle of the final state electron with respect to the neutrino, θ , is uniquely determined from the initial neutrino and final lepton energies by

$$1 - \cos\theta = \frac{m_e(1-y)}{E_e}; \quad (2)$$

therefore at accelerator neutrino energies, where $m_e \ll E_\nu$, the final state electron is very forward. Electroweak radiative corrections for these cross sections have been calculated to one loop [1] and constitute few-percent corrections to the tree-level expressions for GeV-energy neutrinos. The prediction can be further improved by including additional low-energy terms due to radiative corrections [2] and one-loop electroweak couplings from recent global fits to electroweak data [3].

Experimental measurements of $\nu_\mu e^-$ and $\bar{\nu}_\mu e^-$ elastic scattering have been performed by the CHARM experiment at CERN [4], the E734 experiment at Brookhaven [5] and, most precisely, by the CHARM-II experiment at CERN [6]. In addition, $\nu_e e^-$ scattering has been studied by the E-225 and LSND experiments at LAMPF [7, 8], and $\bar{\nu}_e e^-$ scattering by the TEXONO experiment [9]. These measurements are limited in precision either by statistics of the neutrino-electron elastic scattering sample, or by knowledge of the incoming neutrino flux, or both.

The theoretical uncertainty of the neutrino-electron scattering cross section is much smaller than the uncertainty associated with any one or the combination of all measurements [3]. This unusual situation in neutrino scattering allows the use of this process as a standard candle from which one can derive constraints on the neutrino flux. The technical challenge that offsets this advantage is that from Eqn.(1) the cross section is small, roughly 10^{-4} of the total charged-current ν_μ cross section, meaning signal statistics are low and backgrounds substantial. However, with an intense neutrino beam and a capable detector, the statistical precision of the neutrino-electron scattering measurement may rival or exceed that of the flux prediction. An *in situ* measurement has the added benefit that it accounts for all effects of the beam optics such as horn current and geometry which can be difficult to predict precisely.

The Neutrinos at the Main Injector (NuMI) beamline at Fermilab [10] has a flux prediction whose precision is limited primarily by uncertainties in the energy and angular spectra of hadrons produced by the incoming proton beam. For the configuration represented by the measurement reported here, the NuMI flux prediction uncertainty ranges from 10% at the 3 GeV peak of the flux, to significantly higher uncertainties above the peak [11, 12]. At the same time, the high intensity of the NuMI beamline means that the total event rate for a neutrino-electron elastic scattering analysis in a multi-

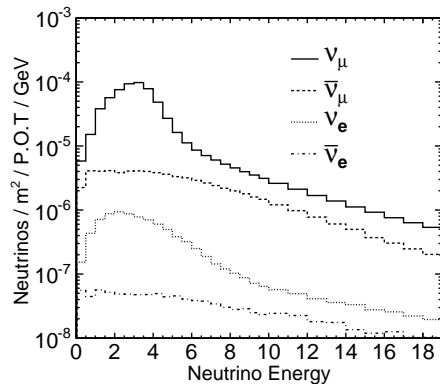


FIG. 1: The predicted flux of ν_μ , $\bar{\nu}_\mu$, ν_e and $\bar{\nu}_e$ for the data used in this analysis.

ton detector has comparable statistical precision to the flux uncertainty.

This article describes a measurement of neutrino-electron scattering using the 6-ton MINERvA scintillator tracking detector. Specifically, the number of these events in the MINERvA detector is measured as a function of electron energy and used to constrain the uncertainty on the NuMI beam flux, which consists primarily of ν_μ . The signature for neutrino-electron scattering is a single electron with energy and angle satisfying $E_e \theta^2 < 2m_e$, given Eqn. 2, and no other activity in the event. The dominant backgrounds come from electrons produced in charged current ν_e and $\bar{\nu}_e$ interactions, and decay photons from π^0 production. Therefore, the analysis selects low angle electrons, rejects photons, and rejects events with any other particles visible in the detector.

The MINERvA experiment uses the NuMI beam [10], which begins with 120 GeV protons striking a graphite target. The mesons produced in $p + C$ interactions are focused by two magnetic horns into a 675 m helium-filled decay pipe. For the data presented here, the horns are set to focus positive mesons, resulting in a ν_μ -enriched beam whose peak energy is 3 GeV. Muons produced in meson decays are absorbed in 240 m of rock downstream of the decay pipe. This analysis uses data taken between November 2010 and April 2012 with 3.43×10^{20} protons on target. The predicted flux of neutrinos for this exposure is shown in Fig. 1, and integrated over all energies, the beam is 92.9% ν_μ , 5.8% $\bar{\nu}_\mu$ and 1.3% ($\nu_e + \bar{\nu}_e$).

The neutrino beam is simulated by a Geant4-based model [13, 14] which is constrained by NA49 proton+carbon hadron production measurements [15]. FLUKA is used to shift NA49 measurements to match NuMI proton energies, which range between 12 and 120 GeV [16, 17]. The π/K ratio measured by MIPP on a thin carbon target [18] is used to constrain production of kaons. Hadronic interactions not constrained by the NA49 or MIPP data are predicted using

the FTFP_BERT hadron shower model implemented in Geant4 version 9.2 patch 3.

The MINERvA detector consists of a core of scintillator bars surrounded by electromagnetic and hadronic calorimeters (ECAL and HCAL, respectively) on the sides and downstream end of the detector. The MINERvA scintillator tracking region is composed of 95% CH and 5% other materials by weight [19]. The strips are perpendicular to the z-axis (which is horizontal and approximately aligned with the beam axis) and are arranged in planes with a 1.7 cm strip-to-strip pitch¹. Three plane orientations ($0^\circ, \pm 60^\circ$ rotations around the z-axis, denoted $X, U,$ and V) facilitate three-dimensional reconstruction of the neutrino interaction vertex and of outgoing charged particle tracks. The 3.0 ns timing resolution of the detector allows separation of particles from multiple interactions within a single beam pulse. MINERvA is located 2 m upstream of the MINOS near detector, a magnetized iron-scintillator tracking spectrometer [20]. Although the latter detector is not used directly in this analysis, it is used to reconstruct the momentum of through-going muons for many calibrations [19] and to perform reconstruction efficiency studies, as described in paragraphs below.

The MINERvA detector's response is simulated by a tuned Geant4-based [13, 14] program, version 9.4 patch 2, with the QGSP_BERT hadron cascade model. The energy scale of the detector is set by ensuring that both the photostatistics and the reconstructed energy deposited by momentum-analyzed through-going muons agree in data and simulation. The calorimetric constants used to reconstruct the energy of electromagnetic showers and correct for passive material are determined from the simulation. The uncertainty in the detector's response to protons and charged pions is constrained by the measurements made with a scaled-down version of the MINERvA detector in a low energy hadron test beam [21]. The energy scale for electrons in the scintillator tracker is verified using a sample of Michel electrons from $\mu^\pm \rightarrow e^\pm \nu \bar{\nu}$ decays of muons stopping in the detector [19], by the reconstructed invariant mass of identified $\pi^0 \rightarrow \gamma\gamma$ decays [22], and in test beam electron measurements [21].

Neutrino interactions are simulated using the GENIE 2.6.2 neutrino event generator [23]. GENIE provides the tree-level neutrino-electron scattering cross section described above, which we modify to account for next-to-leading-order radiative corrections as described in the Appendix. For quasielastic ν_e interactions, the cross section is given by the Llewellyn Smith formalism [24]. Vector form factors come from fits to electron scattering data [25]; the axial form factor used is a dipole with an

axial mass (M_A) of $0.99 \text{ GeV}/c^2$, consistent with deuterium measurements [26, 27], and sub-leading form factors are assumed from PCAC or exact G-parity symmetry [28]. The nuclear model is the relativistic Fermi gas with a Fermi momentum of $221 \text{ MeV}/c$ and with an extension to higher nucleon momenta to account for short-range correlations [29, 30]. Inelastic reactions with a low hadronic invariant mass are based on a tuned model of discrete baryon resonance production [31], and the transition to deep inelastic scattering is simulated using the Bodek-Yang model [32]. Final state interactions are modeled using the INTRANUKE package [23]. Coherent pion production is simulated using the model of Rein and Sehgal [33]. Uncertainties in the parameters of these models are assigned according to uncertainties in experimental measurements or to cover differences between experiments and model predictions.

The MINERvA detector records the energy and time of energy depositions (hits) in each scintillator bar. Hits are first grouped in time and then clusters of energy are formed by spatially grouping the hits in each scintillator plane. Clusters with energy $> 1 \text{ MeV}$ are then matched among the three views to create a track. An electron typical of a $\nu e \rightarrow \nu e$ scatter features a single particle track near the neutrino interaction vertex at which it was created, gradually developing into an electromagnetic cascade in the scintillator and terminating in the downstream electromagnetic calorimeter. An energetic electron typically traverses at least one radiation length as a minimum-ionizing particle (MIP) until it begins to shower. The 40 cm radiation length of scintillator corresponds to 25 planes when the direction of the electron is normal to the planes. The MIP-like segment can be identified as a track, and the beginning (angle) of that track serves as the event vertex (electron angle). Occasionally, an electron starts to shower early and the MIP track is too short to be reconstructed as a track. In this case the topologically contiguous energy deposition is used in a least-squares fit to define the vertex location and shower direction which are inputs to the cone algorithm described below. Only events with an event vertex within the central 112 planes of the scintillator tracking region and no closer than 4 cm to any edge of the central tracker are retained as signal candidates. These requirements define a region with a mass of 6.10 metric tons.

Once a track or an isolated energy deposition is identified, a search cone is formed using the vertex and angle of the identified object. The cone is defined to have an opening angle of 10 degrees with respect to the electron direction, and it begins at a location upstream of the vertex such that the width of the cone 80 mm upstream of the vertex is 50 mm. The cone extends far enough to capture the downstream remnants of the electromagnetic showers which sometimes fluctuate to only a single photon which later converts. The energy within the search cone is summed according to the calorimetric tuning as

¹ The y-axis points along the zenith and the beam is directed downward by 58 mrad in the y-z plane.

defined above; this is identified as the electron candidate energy. The resulting electron fractional energy resolution using this procedure is $5.9\%/\sqrt{E_e/\text{GeV}} \oplus 3.4\%$ [34].

Accurate reconstruction of the electron shower direction is critical to the rejection of backgrounds using an $E_e\theta^2$ cut, as discussed below. The energies and locations of clusters inside the cone are fed into a Kalman filter to determine the electron angle with respect to the beam direction. Because the downstream end of an electron shower does not necessarily align with the original electron direction, only the most upstream 30 clusters are used in the fit. The resulting average electron angular resolution is 7.2 (7.5) mrad in the horizontal (vertical) direction [34].

The event interaction time is inferred from the times of the tracked hits. Other (untracked) clusters that are within 20 ns before and 35 ns after that time are also associated with the event. Energy within this reconstruction time window, but outside the electron cone, is used to search for the presence of other particles in the event which would indicate that the event is a background rather than neutrino-electron elastic scattering event.

The majority of neutrino interactions in MINERvA come from charged-current (CC) ν_μ interactions on nuclei either in or upstream of the detector. Events truly originating upstream of the fiducial volume but reconstructed within it can be rejected simply by requiring the energy in a 30 cm-diameter cylinder along the cone axis and upstream of the reconstructed event vertex be less than 300 MeV. True fiducial ν_μ CC events, on the other hand, can be identified by the presence of a muon or other MIP-like charged particle, which will frequently penetrate through the ECAL into the HCAL, in contrast to electron showers, which typically end in the ECAL. Events are removed if the end of the shower penetrates through more than 2 planes of the hadron calorimeter, which corresponds to 5 cm of steel and 3 cm of scintillator, or 3 radiation lengths for normally incident particles.

After the ν_μ CC interactions on nuclei are removed, the remaining background is from neutral-current (NC) pion production or electron neutrino interactions on nuclei in the detector. These topologies are removed with a series of cuts described below.

A minimum energy of 0.8 GeV is required to remove the significant background that arises from π^0 decays to photons and to ensure good angular and energy reconstruction of the electron. In addition, the electron track is not allowed to bend by more than 9 degrees, since this would indicate a hadronic scatter. To ensure that the search cone contains the energy of only one particle, cuts are made on the transverse and longitudinal energy distributions and on the consistency of the energy depositions between the three views of the scintillator planes.

Two transverse energy cuts are made to remove two-particle backgrounds. Firstly, the energy within 5 cm of

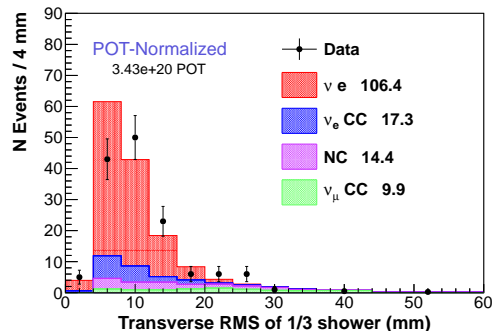


FIG. 2: The energy-weighted RMS of the transverse distance of each cluster of energy from the cone center, averaged over the planes in the first third of the shower for data and simulation, after the simulated backgrounds have been tuned.

the outer boundary of the electron cone is required to be less than 120 ($65 + 7.8 \times E_e/\text{GeV}$) MeV for electrons that are less (greater) than 7 GeV in energy. Secondly, for each view, the energy-weighted RMS of the distances of each cluster from the cone center in the first third of the shower must be less than 20 mm. The distribution of events for data and simulation, after the background tuning discussed below and after all cuts but this one are made, is shown in Fig. 2.

Cuts are also made on the longitudinal energy distribution to ensure that the shower is from a single electromagnetic particle. The Kalman filter that determines the electron angle returns a χ^2 describing the quality of the fit to a single-particle energy deposition. A very loose cut requiring the χ^2 per number of degrees of freedom to be less than 100 is made to remove multiple particle showers without compromising the single-particle acceptance. In addition, the longitudinal position of the plane containing the maximum energy deposition must be at a distance from the shower start that is consistent with electromagnetic shower propagation in scintillator. This removes two-photon events since the two photons, even if overlapping in space, will not usually convert at the same point.

Finally, the energy deposition in the search cone for each view relative to the other two views is required to be consistent with that of a single particle. When there are two or more particles originating from the same vertex, they will rarely overlap in more than one detector view. Because there are twice as many planes in the X orientation as in the U or V orientation, the following two cuts remove events where two or more particles overlap inside the cone in one view but not all views:

$$\left| \frac{E_X - E_U - E_V}{E_X + E_U + E_V} \right| < 0.28,$$

$$\left| \frac{E_U - E_V}{E_U + E_V} \right| < 0.5.$$

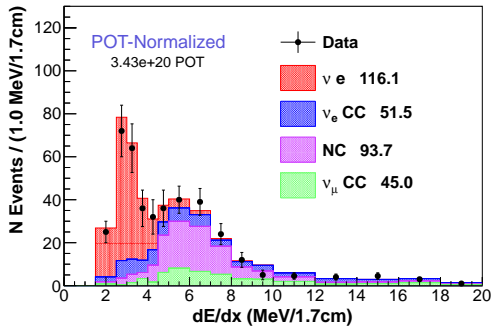


FIG. 3: The distribution of dE/dx after the cuts that isolate single electromagnetic showers are made and after the background has been tuned, but before the final dE/dx cut is made. Signal candidates are required to have an average dE/dx less than 4.5 MeV / 1.7 cm.

Here, E_J is the energy deposited in the J plane orientation of the detector.

After the cuts above, the remaining backgrounds are primarily from ν_e quasielastic interactions, and single-photon events. Photons can be rejected by looking at the energy deposition per unit distance (dE/dx) at the beginning of the electron candidate track. For photons that convert, dE/dx is consistent with that made by two electrons while the signal dE/dx is that of only one electron. The cut is best made before the electron starts showering, but far enough into the track that the photostatistics are adequate. The optimal distance for this analysis is to cut on the average energy deposition in the first four scintillator planes of the track. This average energy deposition, normalized by the cosine of the incident electron, is shown for data and predicted signal and background events in Fig. 3. Signal events are required to have an average dE/dx less than 4.5 MeV / 1.7 cm, where 1.7 cm corresponds to the thickness of one scintillator plane.

After the dE/dx cut is made the remaining major background is from ν_e charged current quasi-elastic interactions (CCQE), namely $\nu_e n \rightarrow e^- p$ or $\bar{\nu}_e p \rightarrow e^+ n$. If the recoiling nucleon is not observed in the detector as is common at low momentum transfer, the final state is a single electron or positron, which cannot be distinguished from the signal using particle identification cuts. Given the kinematics described by Eqn. 2 and the small angle approximation, $E_e \theta^2$ must be less than the electron mass for neutrino-electron scattering, but is usually much larger for neutrino-nucleon scattering. Figure 4 shows the distribution of this quantity for the data, and the signal and background predictions, after all cuts except the $E_e \theta^2$ cut. Events with $E_e \theta^2$ greater than 0.0032 GeV radian² are removed.

The $E_e \theta^2$ cut removes the ν_e CCQE background effectively at low energy, but it is less effective for high en-

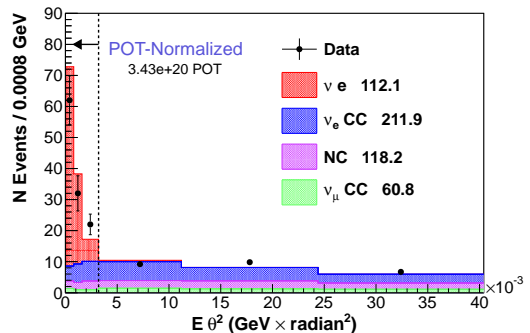


FIG. 4: The distribution of $E_e \theta^2$ for data and simulation after the backgrounds have been tuned to sidebands and after all cuts except the $E_e \theta^2$ cut are made. The signal region is defined as the events with $E_e \theta^2$ less than 0.0032 GeV radian².

ergy electrons because those electrons are also produced at smaller angles, as in neutrino-electron scattering. An additional cut on the momentum transfer squared, Q^2 , reconstructed directly under the assumption of ν_e CCQE kinematics, is applied, where

$$E_\nu = \frac{m_n E_e - m_e^2/2}{m_n - E_e + P_e \cos \theta}, \quad (3)$$

$$Q^2 = 2m_n(E_\nu - E_e), \quad (4)$$

where m_n is the neutron mass. Events with Q^2 less than 0.02 GeV² are removed to reject high energy electron ν_e CCQE events.

After all the cuts are made, there are a total of 127 candidates, with $30.4 \pm 2.3(stat) \pm 3.3(syst)$ predicted background events. The resulting electron energy spectrum is shown in Fig. 5. The simulation indicates that the product of acceptance and efficiency averaged across electron energy is $73.3 \pm 0.5\%$ and varies between approximately 70% at the lower and upper ends of the spectrum and 78% at moderate electron energies. The electron energy spectrum after correction for acceptance and efficiency is shown in Fig. 6. The total number of background-subtracted, efficiency-corrected events is 135.3 ± 17 .

As shown in Fig. 4, the number of predicted background events after the final event selection is a small fraction of the signal events. To produce the signal electron energy distributions, the backgrounds must be estimated and subtracted. This procedure is subject to systematic uncertainties because mis-modeling of both the background and the neutrino flux can bias the signal measurement.

To reduce the background prediction uncertainty and the dependence of the backgrounds on the *a priori* flux prediction, the analysis normalizes the background prediction using events that fail the $E_e \theta^2$ cut but still pass a looser dE/dx cut. The sideband is defined to be all events with $E_e \theta^2$ greater than 0.005 GeV radian² and dE/dx less than 20 MeV/1.7cm. This region is chosen

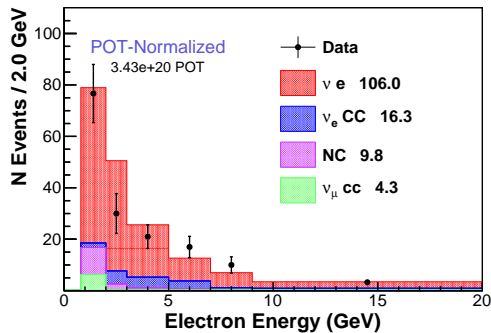


FIG. 5: The electron energy distribution for the data (black points) and predicted signal and backgrounds (stacked histograms) after all the cuts described in the text are made, and after the background tuning procedure is complete. Radiative corrections to the $\nu_e \rightarrow \nu_e$ prediction (described in the Appendix) have been applied.

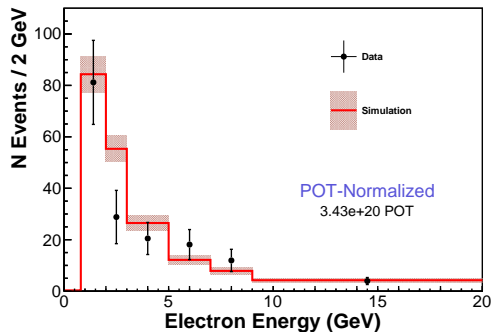


FIG. 6: The electron energy distribution for the data (black) and simulation (red) after all backgrounds are subtracted and after efficiency correction. Radiative corrections to the $\nu_e \rightarrow \nu_e$ prediction (described in the appendix) have been applied to the simulation.

with a sufficiently high $E_e\theta^2$ value so that it contains no signal events but has a low enough dE/dx value to contain only events similar to those that populate the signal region.

However, this sideband still contains several different background sources whose models are poorly constrained by other data and must be extrapolated into the signal region. The backgrounds are classified as ν_e events, ν_μ charged current (CC) interactions, and ν_μ neutral current interactions, including coherent π^0 production. This sideband is divided into three distinct regions in order to determine overall normalizations for three different background sources. The cuts on the shower end transverse position and the fiducial track length in the hadron calorimeter are removed so the distributions of those observables can be fit over their full ranges.

The first region contains events with dE/dx above 3 MeV/1.7cm. Because this sideband tends to have more neutral pions, it has roughly half its events from ν_μ CC

events, and a third of its events are NC events, with only one sixth expected from from ν_e events. The other two regions have dE/dx below 3 MeV/1.7cm but are differentiated by having an electron energy above or below 1.2 GeV. The region with low energy electron candidates is contaminated by ν_μ CC events. With almost three quarters ν_μ CC events, this sideband has only a few per cent ν_e and one quarter ν_μ NC and NC coherent π^0 production. The third region, which has low dE/dx but high electron energy, is about half ν_e events, with the remainder split between ν_μ CC and NC events. In the ν_e -enhanced third region the maximum transverse RMS among the three views is also included in the fit for additional sensitivity to electrons.

The power of this procedure comes from the fact that the different backgrounds occur in substantially different fractions in each of the three regions. Because no region of the sideband contains an appreciable fraction of NC coherent π^0 events, the simulation's prediction for this background cannot be constrained; it is subtracted without modification.

A χ^2 is formed over all of the distributions and is minimized, allowing three overall background normalizations to float. The fit returns normalization constants of 0.76 ± 0.03 for the ν_e backgrounds and 0.64 ± 0.03 (1.00 ± 0.02) for the ν_μ neutral (charged) current backgrounds. After the fit there is good agreement between the data and simulation for all the distributions used in the fit. In addition, both the dE/dx and $E_e\theta^2$ distributions are well-reproduced in the sideband regions after fitting.

The systematic uncertainties on the electron energy distribution are classified as either the uncertainties in the background prediction or the uncertainties in the detector efficiency and acceptance. Contributions to the systematic uncertainty in the backgrounds are shown in Fig. 7; they are evaluated by changing the underlying simulation prediction according to the various uncertainties, refitting the background scale factors, and then subtracting the background, extracting the electron energy spectrum, and correcting for detector acceptance.

The largest uncertainty in the background prediction comes from the background cross section models, although it is significantly reduced by the sideband tuning procedure described above. The dominant systematic uncertainty for electron energies below 7 GeV comes from the fact that the ν_e CCQE cross-section shape as a function of Q^2 is not known precisely, and for those electron energies the background at low Q^2 must be extrapolated using events at high $E_e\theta^2$, which are also at high Q^2 . MINERvA measured a different ν_μ cross section shape versus Q^2 than what is in the standard GENIE neutrino event generator [35], and the systematic is evaluated by taking the difference between the shape of the cross section as a function of Q^2 that MINERvA measured and the one predicted by GENIE. There is a recent mea-

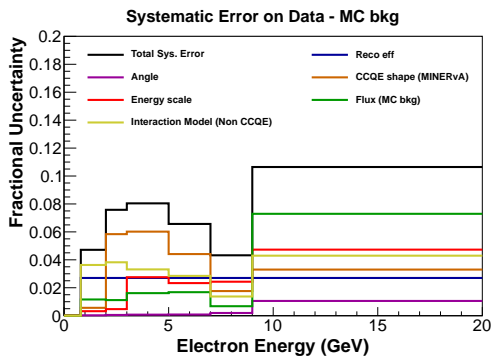


FIG. 7: The fractional systematic uncertainties as a function of the electron energy after all the cuts described above are made, and after the tuned background has been subtracted.

surement of the ν_e CCQE cross-section shape [36] that shows that within one standard deviation, the ν_e and ν_μ cross-section shapes are consistent with one other. At higher electron energies, because of the minimum Q^2 cut, this uncertainty no longer dominates and the flux and the electron energy scale become the largest uncertainties. The flux uncertainties, which contribute primarily to the coherent background subtraction, are incorporated by varying the parameters associated with hadron production and beam focusing in the flux model. The non-CCQE interaction model uncertainties are evaluated by varying the underlying parameters in the cross-section models for processes such as resonance production and coherent scattering.

The largest uncertainty in the detector efficiency and acceptance comes from the uncertainty in the electron energy scale (4%), which is determined by comparing the agreement between data and simulation for the Michel electron candidates. The applicability of this energy scale across a wide array of energies and for electromagnetic showers is confirmed using samples of $\pi^0 \rightarrow \gamma\gamma$ decays [22] and Michel electrons from $\mu^\pm \rightarrow e\nu\bar{\nu}$ decays of muons stopping in the detector [19], as well as in test beam measurements using a smaller version of the MINERvA detector [21].

The remaining detector-related uncertainties are associated with the electron angle reconstruction and tracking efficiency. The uncertainty in the neutrino beam angle direction with respect to the detector axis (1 mrad) is evaluated by comparing the data and simulation for high energy ν_μ charged current events that have very low hadronic energy. Based on that comparison, a correction of 3(1) mrad is made on the angle in the vertical (horizontal) direction. The reconstruction efficiency uncertainty is estimated by assuming that the uncertainty for electrons is the same as it is for muons, since both particles' tracks are seeded using the same technique. The reconstruction efficiency uncertainty for muons is determined by comparing the data and simulation for the efficiency

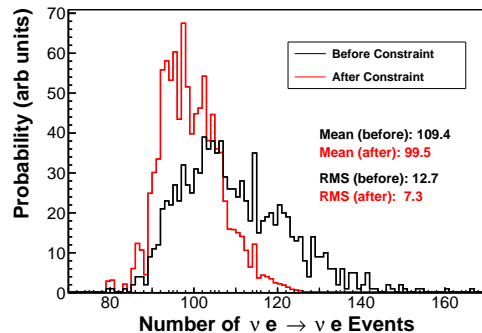


FIG. 8: The probability distribution (black) of the predicted number of neutrino-electron scattering events in the simulation given errors in the neutrino flux model and the modified probability distribution (red) given the observed electron energy spectrum.

of matching a muon track in MINERvA once a track is found in MINOS that extrapolates into MINERvA. The discrepancy between data and simulation is treated as the systematic uncertainty.

The final state electron energy spectrum can constrain both the overall normalization and the shape of the neutrino flux. Bayes' theorem relates the probability of a particular flux model (M) given an observed electron spectrum ($N_{\nu e \rightarrow \nu e}$) to the *a priori* probability of the model and the probability of the data given the model:

$$P(M|N_{\nu e \rightarrow \nu e}) \propto P(M)P(N_{\nu e \rightarrow \nu e}|M). \quad (5)$$

Assuming a Gaussian approximation of the Poisson-distributed data, the probability of the data spectrum given the model is proportional to:

$$P(N_{\nu e \rightarrow \nu e}|M) \propto e^{-\chi_M^2}, \quad (6)$$

where χ_M^2 is the chi-square statistic comparing the observed electron energy distribution to that predicted by model M . This procedure assumes that the probability to see at least the difference between the mean prediction and the actual measurement is not negligibly small.

Figure 8 shows the *a priori* probability distribution of the number of neutrino-electron scattering events predicted, obtained by randomly varying parameters of the flux simulation within uncertainties to create many flux “universes”, each with a different predicted neutrino-electron scattering spectrum. The uncertainties in the flux simulation come from hadron production measurements, uncertainties in the beamline focusing system and alignment [37], and comparisons between different hadron production models in regions not covered by the NA49 or MIPP data. Also shown in Fig. 8 is the probability distribution given the observed neutrino-electron scattering spectrum. This is constructed by weighting the entry corresponding to a given universe by $e^{-\chi_i^2}$,

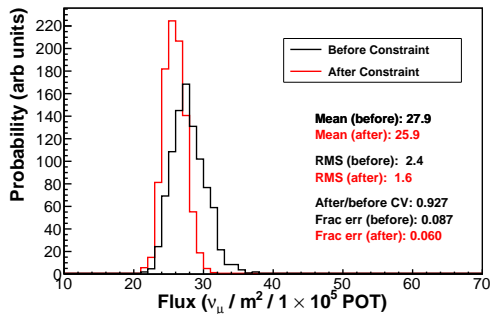


FIG. 9: The probability distribution (black) of the predicted ν_μ flux integrated between 2 and 10 GeV given errors in the neutrino flux model and the modified probability distribution (red) given the observed electron energy spectrum.

where the exponent evaluates the difference between the predicted neutrino-electron scattering energy spectrum in universe i and that observed in the data. The mean of the second, “constrained”, distribution is 9% lower than that of the original distribution, and the RMS is reduced by 40%.

The same weights applied to produce this distribution can be used to constrain any other quantity that is calculable by the simulation and varies depending on the flux prediction. For instance, the ν_μ flux integrated between 2 and 10 GeV can be calculated both before and after the constraint: that probability distribution is shown in Fig. 9. The mean of the constrained probability distribution is lower by 7% compared to the distribution before the neutrino-electron scattering constraints. The ν_μ flux as a function of neutrino energy before and after the constraint is shown in Fig. 10. The error on this flux, defined as the RMS of the predictions for each neutrino energy bin, before and after the constraint are shown in Fig. 11. Because of the correlations between the ν_μ and $\nu_e + \bar{\nu}_e$ fluxes through the $\pi \rightarrow \nu\mu, \mu \rightarrow \nu_e, \bar{\nu}_\mu$ chain, this technique can also be used to constrain those fluxes, for example in Ref. [36], which uses a constrained prediction for the ν_e and ν_μ fluxes to more accurately measure the ν_e CCQE cross section.

The method described above can be used directly by any other experiment employing the NuMI beam as a neutrino source, regardless of its position or orientation with respect to the beam axis. To do this, all that is required as input is the predicted number of neutrino-electron scattering events with $E_e > 800$ MeV in a volume and mass corresponding to the MINERvA detector and the same integrated protons on target, distributed according to the assumed uncertainties on the flux prediction. This should then be compared to the measured efficiency-corrected number of events reported by MINERvA. The MINERvA detector’s number of target electrons, location along the NuMI beamline, and volume are given in Table I.

E_e (GeV) range	0.8 – 2	2 – 3	3 – 5	5 – 7	7 – 9	9 – ∞
νe events	48.7	14.4	20.5	18.1	11.9	21.6
in range	± 9.9	± 5.2	± 6.3	± 5.9	± 4.3	± 7.7
0.8 – 2	98.7	1.22	1.72	1.38	0.420	-0.269
2 – 3	1.22	27.3	1.63	1.14	0.340	0.755
3 – 5	1.72	1.63	40.1	1.88	0.596	1.35
5 – 7	1.38	1.14	1.88	34.7	0.448	0.968
7 – 9	0.42	0.340	0.596	0.448	18.9	0.778
9 – ∞	-0.269	0.755	1.35	0.968	0.778	59.5

TABLE I: The acceptance-corrected number of $\nu e^- \rightarrow \nu e^-$ events in bins of electron energy, their uncertainties, and their covariance matrix. The MINERvA detector mass can be represented by a hexagonal prism with face apothem 88.125 cm and length 2.53 m, oriented with its axis tilted 58 mrad upward from the NuMI beam axis, consisting of $1.98 \pm 0.03 \times 10^{30}$ electrons spread uniformly throughout (a fiducial mass of 6.10 tons). This volume should be centered at a point 1031.7 m from the upstream edge of the first focusing horn in the NuMI beamline and 0.264 m (0.129 m) away from the neutrino beam horizontal (vertical) axis in the positive (positive) direction.

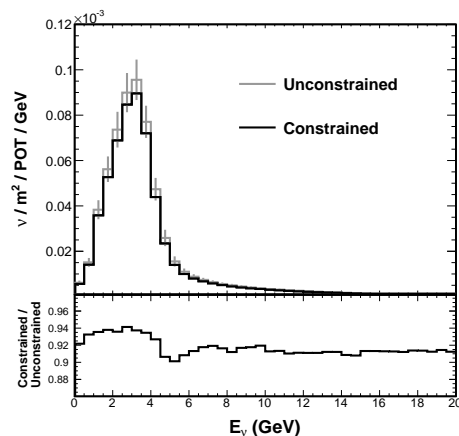


FIG. 10: The ν_μ flux prediction for the NuMI beamline, before (gray) and after (black) the neutrino-electron scattering flux constraint (top) and the ratio of the constrained to unconstrained predictions (bottom).

This measurement is also an important proof-of-principle for a technique that could be used for a future long baseline neutrino experiment, such as the DUNE [38] experiment. The process, because it involves scattering off electrons rather than nuclei, provides a precise flux prediction given any near-detector technology with sufficient angular resolution, energy reconstruction and mass to isolate a statistically significant sample of these events.

This work was supported by the Fermi National Accelerator Laboratory under US Department of Energy contract No. DE-AC02-07CH11359 which included the MINERvA construction project. Construction support also was granted by the United States National Science Foundation under Award PHY-0619727 and by the University of Rochester. Support for participating scientists

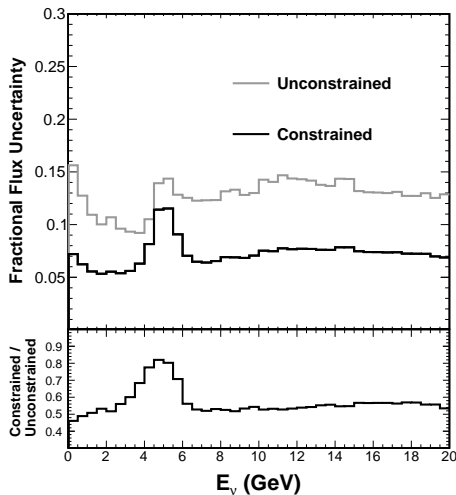


FIG. 11: The error on the ν_μ flux prediction for the NuMI beamline, before (gray) and after (black) the neutrino-electron scattering flux constraint (top) and the ratio of the constrained to unconstrained errors (bottom).

was provided by NSF and DOE (USA) by CAPES and CNPq (Brazil), by CoNaCyT (Mexico), by CONICYT (Chile), by CONCYTEC, DGI-PUCP and IDI/IGI-UNI (Peru), by Latin American Center for Physics (CLAF) and by RAS and the Russian Ministry of Education and Science (Russia). We thank the MINOS Collaboration for use of its near detector data. Finally, we thank Fermilab for support of the beamline and the detector, and in particular the Scientific Computing Division and the Particle Physics Division for support of data processing.

* now at SLAC National Accelerator Laboratory, Stanford, California 94309 USA

† Now at Illinois Institute of Technology

‡ now at University of Michigan, Ann Arbor, MI, 48109

§ also at Department of Physics, University of Antananarivo, Madagascar

¶ now at Fermi National Accelerator Laboratory, Batavia, IL USA 60510

** Now at Tufts University, Medford, Massachusetts 02155, USA

- [1] S. Sarantakos, A. Sirlin, and W. Marciano, *Nucl.Phys.* **B217**, 84 (1983).
- [2] J. N. Bahcall, M. Kamionkowski, and A. Sirlin, *Phys.Rev.* **D51**, 6146 (1995), arXiv:astro-ph/9502003 [astro-ph] .
- [3] J. Erler and S. Su, *Prog.Part.Nucl.Phys.* **71**, 119 (2013), arXiv:1303.5522 [hep-ph] .
- [4] J. Dorenbosch *et al.* (CHARM), *Z.Phys.* **C41**, 567 (1989).
- [5] L. Ahrens, S. Aronson, P. Connolly, B. Gibbard, M. Murtagh, *et al.*, *Phys.Rev.* **D41**, 3297 (1990).
- [6] P. Vilain *et al.* (CHARM-II), *Phys.Lett.* **B335**, 246 (1994).

- [7] R. Allen, H. Chen, P. Doe, R. Hausammann, W. Lee, *et al.*, *Phys.Rev.* **D47**, 11 (1993).
- [8] L. Auerbach *et al.* (LSND), *Phys.Rev.* **D63**, 112001 (2001), arXiv:hep-ex/0101039 [hep-ex] .
- [9] M. Deniz *et al.* (TEXONO), *Phys.Rev.* **D81**, 072001 (2010), arXiv:0911.1597 [hep-ex] .
- [10] P. Adamson *et al.*, (2015), arXiv:1507.06690 [physics.acc-ph] .
- [11] L. Fields *et al.* (MINERvA), *Phys. Rev. Lett.* **111**, 022501 (2013), arXiv:1305.2234 [hep-ex] .
- [12] P. Adamson *et al.* (MINOS), *Phys. Rev.* **D77**, 072002 (2008), arXiv:0711.0769 [hep-ex] .
- [13] S. Agostinelli *et al.*, *Nuclear Instruments and Methods in Physics Research Section A: Accelerators, Spectrometers, Detectors and Associated Equipment* **506**, 250 (2003).
- [14] J. Allison *et al.*, *Nuclear Science, IEEE Transactions on* **53**, 270 (2006).
- [15] C. Alt *et al.* (NA49 Collaboration), *Eur.Phys.J.* **C49**, 897 (2007), arXiv:hep-ex/0606028 [hep-ex] .
- [16] A. Ferrari, P. R. Sala, A. Fasso, and J. Ranft, (2005).
- [17] G. Battistoni, S. Muraro, P. R. Sala, F. Cerutti, A. Ferrari, *et al.*, *AIP Conf.Proc.* **896**, 31 (2007).
- [18] A. V. Lebedev, *Ratio of pion kaon production in proton carbon interactions*, Ph.D. thesis, Harvard University (2007).
- [19] L. Aliaga *et al.* (MINERvA), *Nucl. Instrum. Meth.* **A743**, 130 (2014), arXiv:1305.5199 [physics.ins-det] .
- [20] D. G. Michael *et al.* (MINOS Collaboration), *Nucl.Instrum.Meth.* **A596**, 190 (2008), arXiv:0805.3170 [physics.ins-det] .
- [21] L. Aliaga *et al.* (MINERvA), *Nucl. Instrum. Meth.* **A789**, 28 (2015), arXiv:1501.06431 [physics.ins-det] .
- [22] T. Le *et al.* (MINERvA), *Phys. Lett.* **B749**, 130 (2015), arXiv:1503.02107 [hep-ex] .
- [23] C. Andreopoulos, A. Bell, D. Bhattacharya, F. Cavanna, J. Dobson, S. Dytman, H. Gallagher, P. Guzowski, R. Hatcher, P. Kehayias, A. Mereaglia, D. Naples, G. Pearce, A. Rubbia, M. Whalley, and T. Yang, *Nuclear Instruments and Methods in Physics Research Section A: Accelerators, Spectrometers, Detectors and Associated Equipment* **614**, 87 (2010), Program version 2.6.2 used here.
- [24] C. H. Llewellyn Smith, *Phys.Rept.* **3**, 261 (1972).
- [25] R. Bradford, A. Bodek, H. S. Budd, and J. Arrington, *Nucl.Phys.Proc.Suppl.* **159**, 127 (2006), arXiv:hep-ex/0602017 [hep-ex] .
- [26] A. Bodek, S. Avvakumov, R. Bradford, and H. S. Budd, *J.Phys.Conf.Ser.* **110**, 082004 (2008), arXiv:0709.3538 [hep-ex] .
- [27] K. S. Kuzmin, V. V. Lyubushkin, and V. A. Naumov, *Eur.Phys.J.* **C54**, 517 (2008), arXiv:0712.4384 [hep-ph] .
- [28] M. Day and K. S. McFarland, *Phys.Rev.* **D86**, 053003 (2012), arXiv:1206.6745 [hep-ph] .
- [29] A. Bodek and J. L. Ritchie, *Phys.Rev.* **D23**, 1070 (1981).
- [30] A. Bodek and J. L. Ritchie, *Phys.Rev.* **D24**, 1400 (1981).
- [31] D. Rein and L. M. Sehgal, *Annals Phys.* **133**, 79 (1981).
- [32] A. Bodek, I. Park, and U.-K. Yang, *Nucl.Phys.Proc.Suppl.* **139**, 113 (2005), arXiv:hep-ph/0411202 [hep-ph] .
- [33] D. Rein and L. M. Sehgal, *Nucl. Phys.* **B223**, 29 (1983).
- [34] J. Park, *Neutrino-Electron Scattering in MINERvA for Constraining the NuMI Neutrino Flux*, Ph.D. thesis, U. Rochester (2013).
- [35] G. A. Fiorentini *et al.* (MINERvA), *Phys. Rev. Lett.* **111**,

- 022502 (2013), arXiv:1305.2243 [hep-ex] .
- [36] J. Wolcott *et al.* (MINERvA), (2015), arXiv:1509.05729 [hep-ex] .
- [37] Z. Pavlovic, *Observation of Disappearance of Muon Neutrinos in the NuMI Beam*, Ph.D. thesis, University of Texas (2008).
- [38] “DUNE collaboration webpage,” <http://www.dunescience.org>, accessed: 2015-11-12.

Appendix: One Loop Electroweak Radiative Corrections to Neutrino-Electron Scattering

The cross-section for tree-level neutrino-electron scattering is given in Eqn. 1, and this is the cross-section implemented in the GENIE 2.6.2 event generator [23] used as the reference model in this analysis. As previously noted, it is necessary to correct this model to use modern values of the electroweak couplings. This is done by changing the chiral couplings, C_{LL} and C_{LR} , to one-loop values predicted using global fits to electroweak data [3]. Table II compares the values for these couplings in GENIE 2.6.2 to the values used in this analysis.

In addition, one-loop electroweak radiative corrections [1, 2] modify the expressions for the $\nu_\mu e$, $\bar{\nu}_\mu e$, $\nu_e e$ and $\bar{\nu}_e e$ elastic scattering cross-sections in Eqn. 1 as follows:

	$C_{LL}^{\nu_e e}$	$C_{LL}^{\nu_\mu e}$	$C_{LR}^{\nu_e e}$
GENIE 2.6.2	0.7277	-0.2723	0.2277
One loop	0.7276	-0.2730	0.2334

TABLE II: Electroweak couplings in GENIE and in our one-loop calculation of νe^- elastic scattering

$$\frac{d\sigma(\nu_\ell e^- \rightarrow \nu_\ell e^-)}{dy} = \frac{G_F^2 s}{\pi} \left[(C_{LL}^{\nu_\ell e})^2 \left(1 + \frac{\alpha_{EM}}{\pi} X_1\right) + (C_{LR}^{\nu_\ell e})^2 (1-y)^2 \left(1 + \frac{\alpha_{EM}}{\pi} X_2\right) - \frac{C_{LL}^{\nu_\ell e} C_{LR}^{\nu_\ell e} m y}{E_\nu} \left(1 + \frac{\alpha_{EM}}{\pi} X_3\right) \right] \quad (7)$$

$$\frac{d\sigma(\bar{\nu}_\ell e^- \rightarrow \bar{\nu}_\ell e^-)}{dy} = \frac{G_F^2 s}{\pi} \left[(C_{LR}^{\nu_\ell e})^2 \left(1 + \frac{\alpha_{EM}}{\pi} X_1\right) + (C_{LL}^{\nu_\ell e})^2 (1-y)^2 \left(1 + \frac{\alpha_{EM}}{\pi} X_2\right) - \frac{C_{LL}^{\nu_\ell e} C_{LR}^{\nu_\ell e} m y}{E_\nu} \left(1 + \frac{\alpha_{EM}}{\pi} X_3\right) \right] \quad (8)$$

where E_ν is the neutrino energy, s is the Mandelstam invariant representing the square of the total energy in

the center-of-mass frame, m is the electron mass and $y = T_e/E_\nu$. The X_i correction terms are

$$X_1 = \frac{1}{12} (6y + 12 \log(1-y) - 6 \log(y) - 5) \log\left(\frac{2E_\nu}{m}\right) - \frac{\text{Li}_2(y)}{2} + \frac{y^2}{24} - \frac{11y}{12} - \frac{1}{2} \log^2\left(\frac{1}{y} - 1\right) + y \log(y) - \frac{1}{12} (6y + 23) \log(1-y) + \frac{\pi^2}{12} - \frac{47}{36} \quad (9)$$

$$X_2 = \frac{(-4y^2 + (-6y^2 + 6y - 3) \log(y) + 11y + 6(1-y)^2 \log(1-y) - 7) \log\left(\frac{2E_\nu}{m}\right)}{6(1-y)^2} + \frac{(-y^2 + y - \frac{1}{2}) \left(\text{Li}_2(y) + \log^2(y) - \frac{\pi^2}{6}\right)}{(1-y)^2} + \frac{(4y^2 + 2y - 3) \log(y)}{4(1-y)^2} - \frac{31 - 49y}{72(1-y)} + \frac{(10y - 7) \log(1-y)}{6(1-y)} + \log(1-y) \left(\log(y) - \frac{1}{2} \log(1-y)\right) \quad (10)$$

$$X_3 = \log\left(-\frac{m}{\sqrt{yE_\nu(2m + yE_\nu)} + m + yE_\nu} + 1 - y\right) \times \left(\frac{(m + yE_\nu) \log\left(\frac{\sqrt{yE_\nu(2m + yE_\nu)} + m + yE_\nu}{m}\right)}{\sqrt{yE_\nu(2m + yE_\nu)}} - 1\right) \quad (11)$$

where $\text{Li}_2(z)$ represents Spence's function, $\int_0^z \frac{-\log(1-u)}{u} du$.